Small Structures

WILEY VCH

RESEARCH ARTICLE OPEN ACCESS

Impact of Halide Alloying on the Phase Segregation of Mixed-Halide Perovskites

Joshua R. S. Lilly[1] | Vincent J.-Y. Lim[1] | Jay B. Patel[2] | Siyu Yan[1] | Jae Eun Lee[1] | Michael B. Johnston[1] | Laura M. Herz[1]

[1]Clarendon Laboratory, Department of Physics, University of Oxford, Oxford, UK | [2]Department of Physics, King's College London, London, UK

Correspondence: Laura M. Herz (laura.herz@physics.ox.ac.uk)

Received: 18 August 2025 | **Revised:** 15 October 2025 | **Accepted:** 20 October 2025

Funding: Engineering and Physical Sciences Research Council, Grant/Award Numbers: EP/Y014952/1 EP/X038777/1 EP/W007975/2

Keywords: halide segregation | metal halide perovskites | solar cells | stability | strain

ABSTRACT

Mixed-halide perovskites are ideal mid- and wide-gap absorbers for multijunction solar cells, but stable photovoltaic performance is severely hampered by halide segregation. This study reveals that crystalline film quality and halide segregation are critically affected by bromide fraction x in $CH_3NH_3Pb(I_{1-x}Br_x)_3$ because of macrostrain and ordered-phase formation. X-ray diffractometry across stoichiometries spanning 22 bromide fractions demonstrates that central compositions near $x = 0.5$ form two macrostrained phases, which exhibit halide segregation under light at different rates. While the overall amplitude of phase segregation follows a broadly symmetric distribution in compositional space, maximized near $x = 0.5$, the potentially ordered compositions of $CH_3NH_3PbIBr_2$ and $CH_3NH_3PbI_2Br$ diverge sharply, presenting particularly stable and unstable scenarios, respectively. Notably, halide segregation is shown to occur even below the widely quoted perceived threshold of $x = 0.2$. Such analysis highlights promising approaches to mitigate halide segregation, through engineering of macrostrained phases and local atomistic ordering. Together, these observations provide crucial benchmarks for proposed models of halide segregation and establish new routes toward segregation-resistant materials for multijunction perovskite-based photovoltaics.

1 | Introduction

Over the past decade and a half, metal halide perovskite (MHP) active layers have been utilized in a range of semiconductor-based devices [1–8]. Notably, the record power conversion efficiency (PCE) for a single-junction MHP-based solar cell has now eclipsed 26% [9]. Excellent optoelectronic properties such as a high charge-carrier mobility, long charge-carrier lifetime, and high absorbance enable this impressive device performance [10–15]. The versatile applicability of MHPs across different semiconductor devices is facilitated by the ease of bandgap tunability of MHPs [16–18]. By altering their chemical composition (ABX_3, where A is a monovalent organic/inorganic cation, B is a divalent metal cation, and X is a monovalent halide anion), in particular via halide alloying, bandgaps across the visible range and into the infrared are accessible [18–25]. While extensive effort has been applied to developing a 1.7 eV MHP to serve as a wide-gap absorber in MHP-Si tandem solar cells, there has been less focus on the optimization of compositions for use in both triple-junction MHP-MHP-Si architectures and multijunction all-perovskite solar cells [9, 18, 26–32]. Such devices could be fabricated monolithically and have higher theoretically accessible PCE values: triple- and quadruple-junction architectures can theoretically exhibit maximum PCEs of 52% and 56%, respectively, under 1-sun illumination [27, 33]. However, to maintain device performance, the stability of each individual absorber must be optimized.

The wide bandgaps required for multijunction perovskite-based solar cells can be achieved by alloying iodide and bromide on the halide X-site of MHPs. However, mixed-halide MHPs undergo halide segregation in the presence of excited charge carriers, generated either via illumination or electronic injection [23, 34, 35]. During segregation, halide ions migrate to establish iodide-rich and bromide-rich regions of the perovskite [36], a process that is reversible once charge carriers are removed [37]. As iodide-rich inclusions possess a smaller bandgap compared to the mixed bulk material, excited charge carriers preferentially funnel to these regions [36, 38, 39]. Such charge-carrier funneling leads to enhanced radiative losses and decreased charge-carrier diffusion lengths, worsening photovoltaic performance [35, 40]. Until now, the majority of studies on halide segregation have each individually focussed on a small number of compositions, and, often, only a single halide ratio [36, 37, 39, 41–45]. Comparing results from different reports is thus hindered by the use of differing processing methodologies and experimental conditions given that extrinsic factors, such as the use of passivating agents and illumination conditions, can affect the material's propensity to segregate [46]. Consequently, it has been challenging to reach a firm conclusion regarding the impact of tuning the bromide-to-iodide ratio, and hence bandgap, on halide segregation dynamics. While some previous studies on adjusting the bromide fraction have been conducted, these have often produced conflicting results [29, 47–54]. For example, while some reports have suggested a possible miscibility gap in the $MAPb(I_{1-x}Br_x)_3$ compositional space (where MA represents methylammonium) [47, 48], others did not substantiate such effects [49, 52]. Importantly, drawing firm conclusions on the effects of iodide-bromide alloying on halide segregation has proven difficult due to the coarse spacings in the range of alloyed halide compositions investigated in the existing literature to date [42, 49]. Fine-tuning of alloy fractions is particularly essential to investigations of material stability near potentially ordered alloy points such as $APbIBr_2$ and $APbI_2Br$, for which predictions of elevated stability have been made [47, 55], or compositions which exhibit significant structural strain, for which lattice deformation could suppress halide segregation [48, 50, 53, 56, 57].

In addition, while several mechanisms for halide segregation have been proposed, there is still no literature consensus on which model most accurately describes the observed, multifaceted, segregation behavior. Direct iodide oxidation [58–60], recombination via charged iodide interstitial defects [41, 61, 62], recombination at crystal lattice distortions via neutrally charged trap states [63, 64], polaron-induced local strain changes [36, 65, 66], and thermodynamic-based bandgap reduction have all been suggested to drive halide segregation [43, 45, 67, 68]. A systematic comparison of segregation behavior across a detailed iodide/bromide compositional space may thus also test the validity of these models, offering solutions to mitigate this detrimental effect.

In this study, we reveal how film microstructure and halide segregation are profoundly affected by changes in the halide ratio for the mixed-halide perovskite $MAPb(I_{1-x}Br_x)_3$. In order to uncover clear differences with composition, we examined an exceptionally finely spaced compositional series, spanning 22 distinct halide compositions. For central compositions with approximately 50% bromide fraction, we find an asymmetric broadening of the X-ray diffraction (XRD) peaks, which we resolve as two constituent subpeaks. We attribute this dual-peak diffraction to the formation of two differently macrostrained phases, which may compensate for the detrimental difference in the iodide and bromide ionic radii and cause the absence of a theoretically predicted [47] miscibility gap. XRD measurements conducted in situ under illumination demonstrate that halide segregation in such central compositions occurs at two different segregation rates, highlighting the potential of initial strain engineering to mitigate segregation. Interestingly, we found the average rate of material segregation to be largely invariant across the compositional series, suggesting that segregation is limited by the halide ion mobility, which tends to show little dependence on halide content [69]. In contrast, we demonstrate that the volume extent or magnitude of halide segregation peaks near the central compositional region around $x = 0.5$. Deviating from this underlying trend, local atomistic ordering within the material is shown to strongly influence the segregation behavior. We experimentally verify the unusual photostability of $MAPbIBr_2$, which had been theoretically predicted previously [47]. In contrast, $MAPbI_2Br$ is revealed to be particularly unstable under light, highlighting its inability to form a photostable ordered structure [47]. The results of this study provide future directions for the development of segregation-resistant compositions for use in multijunction perovskite-based solar cells and offer a clear benchmark for the testing of models aiming to explain the mechanism underlying halide segregation.

2 | Results

2.1 | Structural Variations Across the Mixed-Halide Series

We begin our study by examining the structural variations across a series of $MAPb(I_{1-x}Br_x)_3$ films through analysis of XRD patterns recorded prior to any significant light exposure having occurred. The full fabrication details for the thin films used in this study are described in Section 5, with all targeted stoichiometries based on an identical processing methodology to enable consistency across the series. We utilize a finely stepped approach across the whole compositional space, with Figure S1 depicting the 22 unique compositions that were targeted, ranging from pure iodide ($x = 0$) through to pure bromide ($x = 1$). For nominal bromide fraction between 0.8 and 0.9, XRD patterns (Figure S2) exhibit broadened peaks with multiple satellites indicating a potential reduction in grain size coupled with compositional inhomogeneities [70]. We attribute this to the mismatch in solubility between Br^-- and I^--based precursors [71]. Further, the film with a nominal bromide fraction of 0.55 shows poor homogeneity as seen in Figures S2 and S3, which is later discussed in more detail. For the remainder of this article, unless otherwise stated, discussion will be limited to halide ratios for which narrow diffraction peaks were obtained (suggesting similar average grain size) and no significant initial compositional inhomogeneity was observed (18 out of 22). For these, Figure 1a highlights the expected lattice parameter decrease (increase in XRD diffraction angle) as the nominal bromide fraction is increased across the compositional series [21, 23].

Intriguingly, closer examination of the second-order diffraction peaks shown in Figure 1a reveals substantial peak asymmetry

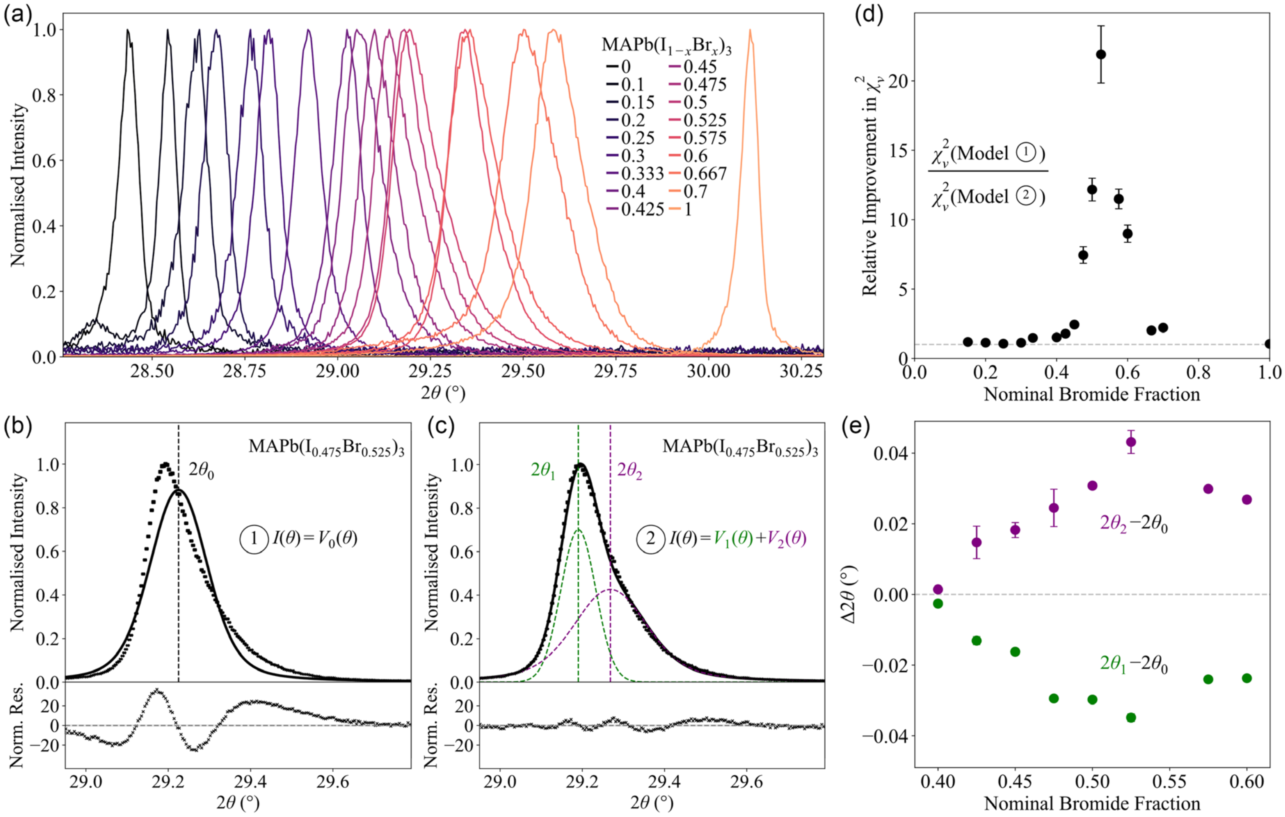

FIGURE 1 | Impact of bromide fraction on the crystal structure of $MAPb(I_{1-x}Br_x)_3$ films. X-ray diffraction patterns were recorded in the dark (prior to any illumination) for unencapsulated films using monochromatic Cu-Kα_1 radiation. (a) Normalized second-order X-ray diffraction peaks for the compositions of interest. For nominal bromide fractions of less than 0.15, (220) and (004) reflections are present, consistent with the expected tetragonal (β) phase [21, 23]. Above this transition point, a single peak resulting from the (200) reflection is present—indicative of the cubic (α) phase. (b) (200) diffraction peak for a film with a nominal bromide fraction of 0.525. Data is modeled with a single Voigt profile, with normalized residuals plotted below. The vertical dashed line indicates the extracted peak center from the fit, labeled as $2\theta_0$. (c) (200) diffraction peak for a film with a nominal bromide fraction of 0.525. Data is modeled with the sum of two Voigt profiles, with normalized residuals plotted below. The vertical dashed lines indicate the extracted peak centers from the fit, with the center of the lower-angle peak labeled in green as $2\theta_1$, and the center of the higher-angle peak marked in purple as $2\theta_2$. (d) Ratio of the minimized reduced χ^2 (χ_ν^2) when a single Voigt profile versus the sum of two Voigt profiles is used to model the (200) diffraction peak. Compositions that crystallized into the tetragonal phase (i.e., $x = 0$ and 0.1) have been omitted. (e) Angular difference, plotted in green (purple), between the low-angle (high-angle) peak position obtained from modeling the (200) peak with the sum of two-Voigt profiles and that obtained from fitting with a single profile, shown for the central bromide region near $x = 0.5$.

for those $MAPb(I_{1-x}Br_x)_3$ films with a bromide fraction near 0.5. As an example of this effect, Figure 1b,c presents the (200) diffraction peak for the film with a nominal bromide fraction of 0.525, highlighting the clear asymmetric nature of the peak profile. To quantify the apparent peak asymmetry present, (200) diffraction profiles across the series were fit with a single Voigt function and the residual evaluated (see Figure 1b). Compositions with a bromide fraction less than 0.15 were not considered for further analysis because of the close proximity of the (220) and (004) reflections. As diffraction measurements can be influenced by both Gaussian and Lorentzian broadening [72, 73], the Voigt function was selected to model the data to ensure generality. We find that for compositions with a bromide fraction suitably far away from 0.5 ($\lesssim$0.4 and $\gtrsim$0.6), a single Voigt function can suitably describe the data (Figure S4), as evidenced by the minimized reduced χ^2 value (labeled χ_ν^2) being close to one (Figures S5 and S6). In addition, residuals are randomly distributed, with a Durbin–Watson statistic ($\mathcal{D}$) approaching two (see Figures S7 and S8) as expected for a high quality fit [74]. However, as demonstrated in Figure 1b, diffraction peaks for films with a bromide fraction close to 0.5 strongly deviate from a single Voigt function (full statistical analysis presented in Figures S5 and S7). This quantitative analysis indicates that for these central compositions, the measured diffraction profile is inconsistent with the material being described by a single lattice parameter [72].

In contrast, we find that the sum of two Voigt functions replicates the observed peak asymmetry across any of the compositions (Figures 1c and S9). Alongside a dramatically reduced normalized residual amplitude, the two-Voigt model shows substantial improvements in χ_ν^2 (Figure S5) and $\mathcal{D}$ (Figures S7 and S8) compared with the single-Voigt model, for the asymmetric peaks observed near $x = 0.5$. To quantify such relative improvement in χ_ν^2, we calculate the ratio of χ_ν^2 values extracted from the two models, which is independent of any uniform error scaling [74]. As Figure 1d shows, films sufficiently rich in a single halide species exhibit a χ_ν^2 ratio close to unity, emphasizing that the (200) peak profile can be described by a single-Voigt function and hence a single lattice parameter. However, in heavily alloyed films, two-Voigt fitting results in a sharp improvement in ${\chi_\nu}^2$ maximizing near 50% bromide inclusion. This striking improvement reveals that, for compositions with a bromide fraction close to 0.5, the (200) diffraction profile is composed of two constituent peaks. We note that a single tetragonal phase could give rise to two closely spaced subpeaks, but we rule out this possibility as the two subpeaks are of similar amplitude (suggesting negligible texturing), while several tetragonally associated reflections are concurrently missing in the XRD patterns. Such peak asymmetry could be caused by the coexistence of two phases with slightly different chemical composition. However, we observe no sudden discontinuity in lattice parameter around $x = 0.5$, and we find that the asymmetry is still present following remixing after halide segregation (see Note S1 for further discussion). We thus propose that the two subpeaks are caused by two different lattice parameters associated with the coexistence of two differently macrostrained material phases. Unlike microstrain, which causes solely a broadening of diffraction peaks, macrostrain manifests as shift in the diffraction peak angles. Thus, two differently macrostrained phases will exhibit slightly displaced diffraction peaks that, when summed, result in the observed asymmetric peak profile (see Note S1 for further discussion) [73, 75].

In order to further examine such compositional regions exhibiting macrostrain, we determined the difference in 2θ between the two constituent peaks of the two-Voigt fits, as visualized in Figure 1e. The angular spacing between the two resolved peaks, and thus, the difference in macrostrain between the two phases, grows toward the central compositional range, maximizing around $x = 0.525$. Previous theoretical and experimental studies have suggested an apparent miscibility gap in the $MAPb(I_{1-x}Br_x)_3$ compositional space, centered close to an x value of 0.5 according to thermodynamic modeling [47, 48]. This miscibility gap was rationalized by considering the substantial ionic radii difference between the halide ions [47, 48]. However, in reality, stabilized mixed-halide structures have been reported across the $MAPb(I_{1-x}Br_x)_3$ series, albeit associated with some XRD peak broadening for bromide fractions close to 0.5 [49, 52]. Here, utilizing a monochromatic incident beam, we are able to resolve that near the center of the compositional range, two differently macrostrained phases form. We postulate that the identified macrostrain can assist in stabilizing the formation of $MAPb(I_{1-x}Br_x)_3$—in effect, the macrostrain compensates for the nonideal difference in halide ionic radii, allowing a stabilized structure to form even when the halide ratio nears 50:50 [53, 56, 76]. The peak in the observed macrostrain (2θ difference, Figure 1e) near a bromide fraction of 0.525 and the inability of the target composition of 0.55 to form a stoichiometrically homogeneous film (Figures S2 and S3) both support this hypothesis. We note that, for single-halide MHPs, macrostrain manipulation has previously been used to stabilize crystal structures [77–81]. Here, we show that intrinsic macrostrain also appears to structurally stabilize mixed-halide films—highlighting a strain engineering strategy for application in multijunction devices.

2.2 | Assessing Halide Segregation Kinetics through XRD Under Illumination

We proceed by investigating how macrostrain and halide alloying affect photostability and halide segregation across the $MAPb(I_{1-x}Br_x)_3$ compositional space. For this purpose, we monitor the evolution of the second-order XRD peak in situ under constant illumination [37, 82]. The $MAPb(I_{1-x}Br_x)_3$ thin films were encapsulated with poly(methyl methacrylate) (PMMA) to negate any atmospheric effects, a low X-ray flux was utilized to avoid material degradation, and thin films were illuminated with low-intensity laser excitation ($0.91\,\mathrm{mW\,cm^{-2}}$ at a wavelength of 470 nm) to minimize any differences in recombination pathway preferences (see Note S2) [63, 83, 84].

First, we examine the rate with which halide segregation evolves across the compositional space, as evidenced from changes in the XRD patterns. Figure 2a contrasts the initial (200) XRD peak with that recorded after 16 h of continuous illumination for $MAPb(I_{0.475}Br_{0.525})_3$ (see Figure S10 for all other compositions). Significant peak broadening is evident, as highlighted by the differential intensity plot in Figure 2b showing the formation of high-angle and low-angle wings during illumination, while the total peak area is conserved (Figure S11), suggesting negligible overall loss of crystalline material. To parameterize the evolution of these changes, we calculated the absolute integral of such differential intensity curves (i.e., the shaded regions above and below the x-axis in Figure 2b) at any given illumination time and normalized these with respect to the peak prior to illumination (see Note S3 for further details).

The extracted time evolution of the relative structural change occurring during illumination is shown in Figure 2c–e for selected compositions (data for all compositions is provided in Figure S12). Remarkably, these curves suggest that the rate of structural change upon illumination is very similar across the wide range of bromide fractions explored (though as discussed further below, the amplitude of the response does vary considerably). To verify this observation, we numerically determined a rate coefficient from the inverse of the time taken for such changes to reach 63% of the final value (see Note S4 for details). The resulting rate coefficients plotted in Figure 2f reveal strikingly similar values across the entire $MAPb(I_{1-x}Br_x)_3$ compositional series. We suggest that the rate-limiting factor in determining the average speed of halide segregation is thus the halide ion mobility, which has been shown to be broadly independent of halide ratio [69].

We note that the dynamic curves capturing the time evolution of the relative structural change can be well described by simple monoexponential rise functions for many compositions (with ${\chi_\nu}^2$ approximately unity, see Figures S12 and S13). However, some divergence from this model is observed for compositions with a bromide fraction close to 0.5. Figure 2c–e illustrates this behavior for three example compositions, with the blue traces representing monoexponential fits to the dynamics of the relative structural change. For the film with a nominal bromide fraction of 0.525 in particular (Figure 2d), the initial rapid rise is followed by a slower, near-linear response at later times, which cannot be captured by the single exponential function. We find that for such central compositions near $x = 0.5$, the dynamics are instead better described by the sum of two exponential rise functions (orange traces, Figure 2c–e and see Figure S12). Figure 2g highlights the relative improvement in the ${\chi_\nu}^2$ fit-quality parameter when moving from fits of a monoexponential function to those of a biexponential function (see Figure S13 for individual ${\chi_\nu}^2$

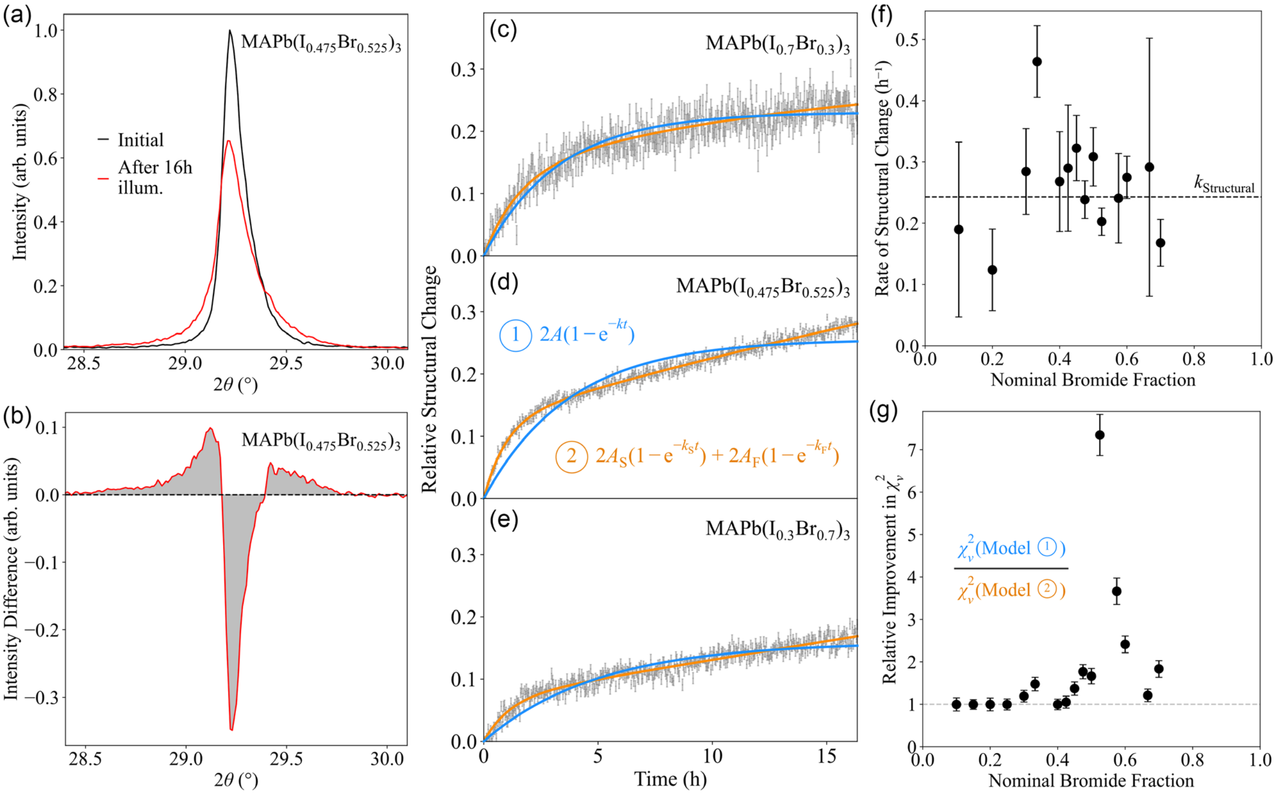

FIGURE 2 | Rate of photoinduced halide segregation probed via X-ray diffraction under illumination (0.91 mW cm^{-2}, 470 nm continuous wave laser light). Diffraction patterns of PMMA-coated $\mathrm{MAPb(I_{1-x}Br_x)_3}$ films were recorded in situ using monochromatic Cu-Kα_1 radiation. (a) (200) diffraction peak before (black trace) and after 16 h (red trace) of continuous illumination for a bromide fraction $x = 0.525$. (b) Intensity difference between the two peaks shown in (a). (c–e) Relative structural change derived from the integral of the absolute value of the differential intensity (e.g., the gray shading, Figure 2b) normalized with respect to the time-zero diffraction profile (further details in Note S3), plotted as a function of illumination time for three example compositions. Fits based on a monoexponential and a biexponential rise function are plotted in blue and orange respectively. (f) Rate coefficient describing the structural change, taken as the inverse of the time taken to reach 63% of the final value (see Note S4 for details). The dashed black line highlights the weighted average rate across all compositions ($k_{\mathrm{Structural}} = (0.24 \pm 0.01)\,\mathrm{h}^{-1}$); 93% of compositions are within two standard error of this value, showing strong statistical agreement with the expected value of 95% [74]. An average rate coefficient could not be extracted for the $x = 0.15$ or 0.25 compositions (see Figure S12 and Note S4 for further details). (g) Ratio of the minimized reduced χ^2 (χ_ν^2) when a monoexponential function versus a biexponential function is used to model the relative structural change evolution.

values). These data show that, while for compositions with either small or large bromide fractions a single rate constant describes the dynamics effectively, two rate constants are required for the central compositions near $x = 0.5$. Interestingly, such findings of two-phase dynamics near $x = 0.5$ (Figure 2g) mirror our prior observation of two differently macrostrained phases in the XRD patterns of unilluminated films for the same compositional region (Figure 1d,e). Previous reports have demonstrated that lattice compression and expansion can modulate the rate of segregation [36, 50, 51, 53, 56, 57, 85, 86]. Here, we therefore argue that such intrinsic macrostrain causes lattice deformation, which leads to two phases exhibiting distinct XRD peaks and segregation kinetics. Recent post-segregation cryogenic scanning transmission electron microscopy measurements appear to support our observations, with “pre-existing strain” being suggested to explain anisotropic segregation behavior [87]. Thus, our finding emphasizes ample opportunities to mitigate halide segregation through control of intrinsic strain, e.g., via compositional engineering or substrate interactions. Such control methods could be further coupled with device-relevant extrinsic techniques to suppress halide ion migration, such as the use of hermetic epitaxial ZnS shells to stabilize mixed-halide nanocrystals for use in perovskite-based light-emitting diodes [88].

2.3 | Absent Threshold for Segregation and the Impact of Ordered Phases

To further elucidate the impact of halide alloying on phase segregation, we now explore how the magnitude of the structural changes varies with bromide content across the $\mathrm{MAPb(I_{1-x}Br_x)_3}$ thin-film series. Interestingly, we find that unlike the segregation rate, which is fairly independent of composition (Figure 2f), the magnitude of change varies significantly and often highly non-monotonically. Figure 3a highlights such effects by showing the relative structural change on a compositional contour map as a function of time under illumination. All compositions were measured under the same conditions (0.91 mW cm^{-2} illumination intensity), and there was no significant sample-to-sample variation for identical compositions (Figure S14). We stress that XRD explores the bulk-averaged structural response of the material; therefore, the relative structural change should mostly reflect

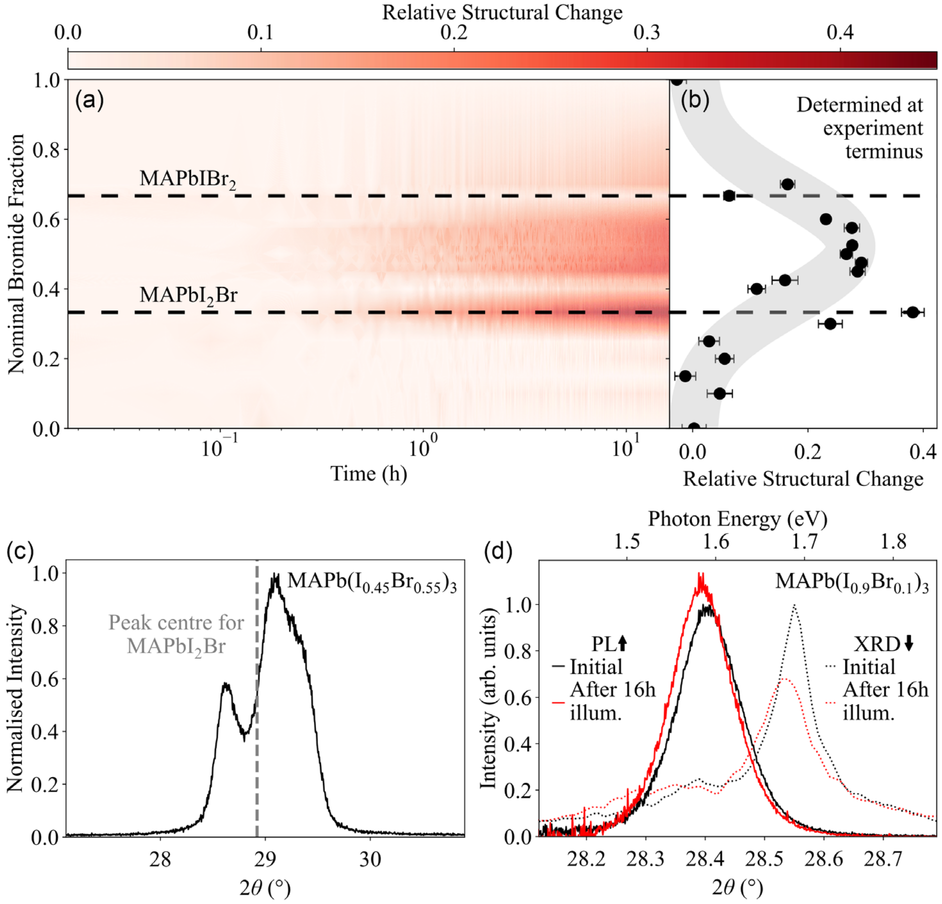

FIGURE 3 | Magnitude of photoinduced halide segregation probed via X-ray diffraction under illumination (0.91 mW cm^{-2}, 470 nm continuous wave laser light). Diffraction patterns of PMMA-coated $MAPb(I_{1-x}Br_x)_3$ films were recorded in situ using monochromatic Cu-Kα_1 radiation. (a) A contour plot of the integral of the relative absolute change in the second-order diffraction peak with respect to time. $MAPbIBr_2$ and $MAPbI_2Br$ are highlighted with a dashed line. Note, measurements on $MAPbI_3$ and $MAPbBr_3$ (segregation impossible) were zero padded from 2 h onward to ensure suitable contrast. (b) Total relative change averaged over the final hour of measurement, together with a Gaussian fit in gray (whose width indicates the estimated $\pm 2\sigma$ uncertainty in the fit calculated at the peak center). As reasoned in the text, the data points for $MAPbIBr_2$ and $MAPbI_2Br$ (dashed lines) were not included in the fitting process. (c) (200) diffraction peak for a thin film with nominal bromide fraction of 0.55 (not PMMA-coated). The angle corresponding to the center of the (200) diffraction peak for $MAPbI_2Br$ is highlighted with a dashed line. (d) Second-order diffraction peak and photoluminescence spectra obtained at illumination onset (black) and after 16 h of illumination (red) for a thin film with a nominal bromide fraction of 0.1.

the volume fraction of material that has undergone halide segregation [37, 49, 63, 64]. We note that changes in photoluminescence have also often been used as a proxy metric for halide segregation [29, 39, 45, 50, 54, 59, 65, 89, 90]. However, such measurements are also affected by charge-carrier funneling and trapping in lower-energy halide-rich domains [40, 64], which will vary considerably with composition because of differences in charge-carrier mobility and bandgap landscape [49, 84, 91]. Therefore, the rate at which segregation occurs and the volume of material that segregates are not directly accessible via photoluminescence spectroscopy. Instead, photoluminescence spectroscopy measurements can act as a simple measure of whether or not some amount of segregation has occurred, though it may not return reliable information on the extent or rate of segregation.

We begin by analyzing the broader trend of material volume segregation across the full composition space, excluding the “special” compositions $MAPbI_2Br$ and $MAPbIBr_2$, which diverge from this general trend and will be discussed further below. For this purpose, we take an average over the values of relative structural change recorded over the final hour of measurement, during which minimal variation is observed. Figure 3b plots such terminus values for the relative structural change, revealing a Gaussian-like distribution across composition (gray shading) centered on a constituent bromide percentage of 52.1% ± 0.5%. This finding demonstrates that the volume susceptibility for segregation is broadly maximal when the constituent bromide and iodide fractions are comparable. Our experimental work is in full agreement with previous theoretical modeling of the compositional phase diagram of $MAPb(I_{1-x}Br_x)_3$ under illumination, which suggested that the region of maximum photoinstability is centered on a bromide fraction of approximately 0.5 [36].

Interestingly, the “special” compositions of $MAPbI_2Br$ and $MAPbIBr_2$, which could potentially support ordered supercell structures, display behavior that sharply diverges from the underlying Gaussian trend. For $MAPbIBr_2$, a sharp reduction in the relative structural change is observed (see dashed line in Figure 3a,b) when compared to neighboring compositions (see Figure S12). It has been theoretically predicted that $MAPbIBr_2$ can indeed form an ordered structure which conveys an enhanced stability against segregation [47]. In the ordered configuration, iodide ions occupy apical sites; the resulting layered structure separates the lead–iodide and lead–bromide bonds along distinct directions, minimizing the Coulomb contribution to the formation energy by minimizing internal strain and promoting stability [47, 55]. Our results thus rationalize recent findings of an MHP with 1:2 iodide-to-bromide ratio yielding a wide-gap absorber for all-perovskite triple-junction solar cells with exceptional stability [27].

Converse to the enhanced segregation resistance of the $MAPbIBr_2$ composition, its iodide-rich counterpart, $MAPbI_2Br$, shows a dramatic decrease in stability under illumination. As Figure 3a,b highlight, the relative structural change increases drastically for $MAPbI_2Br$ (and the nearby composition with bromide fraction $x = 0.3$) with respect to the underlying Gaussian trend. The large discrepancy in volume segregation for $MAPbI_2Br$ and $MAPbIBr_2$ can be directly visualized in Figure S10 by comparing the diffraction peaks for both materials before and after light soaking. From thermodynamic considerations, unlike $MAPbIBr_2$, $MAPbI_2Br$ is not expected to be able to form an ordered structure that exhibits a negative energy of mixing [47]. Previous theoretical work suggests that the use of the symmetry-breaking organic cation prevents the formation of a stable $MAPbI_2Br$ phase [47, 55]. Further evidence for the instability of the $MAPbI_2Br$ phase is given in Figure 3c, which depicts the (200) diffraction peak (no illumination) of a $MAPb(I_{1-x}Br_x)_3$ film with a nominal x value of 0.55. For this composition, a broad and non-uniform peak is observed, indicative of significant compositional inhomogeneity. Interestingly, rather than exhibiting symmetric broadening, a clear local minimum is formed in the diffraction peak, situated close to the diffraction peak center associated with the unstable $MAPbI_2Br$ composition. These observations provide further evidence of the instability of the 1/3 bromide composition, as other compositions in the vicinity clearly form more favorably.

Finally, we explore the commonly held belief that halide segregation only occurs in mixed-halide perovskites with a bromide fraction exceeding 0.2 [35, 56–58, 92, 93]. Much photovoltaic device research has been focussed on compositions below this threshold under the assumption that these do not exhibit halide segregation [46, 89, 90, 94]. However, we find that discernible signatures of structural change are evident in Figure 3a even for $MAPb(I_{1-x}Br_x)_3$ films below the x = 20% threshold. As an example, Figure 3d plots the second-order diffraction peak before and after 16 h of light-soaking for a film with a nominal bromide fraction of 0.1, which exhibits a shift to low angle and the emergence of a low-angle tail, indicative of the formation of iodide-rich perovskite (the total peak area shows no discernible change, Figure S11). Furthermore, photoluminescence spectra recorded simultaneously at the beginning and end of illumination evidence a small redshift and an increase in the PL intensity (Figure 3d), typical of halide segregation [34, 39, 63]. Thus, we clearly show via simultaneous structural and optical probes that, while the extent of halide segregation is relatively low for low bromide content, there is no hard threshold for segregation at the bromide fraction of 0.2.

3 | Discussion

We note that our fine-grained compositional study provides a wealth of benchmarks against which models of halide segregation can be tested and refined. The current range of models proposed is exceptionally wide, ranging from direct iodide oxidation [58–60], to charge recombination via iodide interstitial defects or crystal lattice distortions [41, 61–64], polaron-induced changes in local strain [36, 65, 66], and thermodynamic models based on bandgap reduction [43, 45, 67, 68]. However, some of these models assume compositional thresholds to exist for halide segregation [45, 58, 68, 91], e.g., governed by direct iodide oxidation or a thermodynamic driving force [58, 91], which our findings suggest to be absent. In addition, the presence of particularly stable ($MAPbIBr_2$) or unstable ($MAPbI_2Br$) configurations must be fully accounted for. Broadly, our findings lend support to models requiring halide segregation to be modulated by some form of lattice strain. For example, the "polaron model" of halide segregation [36, 66] suggests that lattice strain generated by a transient polaron is able to stabilize compositional fluctuations that, when relatively iodide-rich, can further funnel additional polarons to subsist stabilization [36, 66]. Such models further predict segregation kinetics to be rate-limited by halide ion migration [66], and a photoinstability profile that is broadly symmetric about an x value of 0.5 [36], in agreement with our findings. The results of our study thus offer a platform for the fine-tuning of such models, with a fully unified model capable of guiding stable material synthesis being the ultimate goal.

Our results also illustrate a variety of design protocols for multijunction perovskite-based photovoltaics (summarized in Table S1). Although the bandgap provided by an $x = 1/3$ mixed-iodide-bromide perovskite may appear ideal for use in a silicon-perovskite tandem solar cell [17], the results of our investigation suggest that this halide mixture is particularly photo-unstable and should be avoided. On the other hand, manipulation of macrostrained phases (for heavily alloyed systems near $x = 0.5$) via strain engineering could be utilized to enhance the stability of top cells in all-perovskite double junctions and silicon-MHP-MHP triple junctions [17, 23, 27, 80, 95, 96]. Finally, the $x = 2/3$ composition is both highly resistant against segregation and exhibits an ideal bandgap for the use as a photostable top cell in all-perovskite triple junctions [27].

4 | Conclusion

In conclusion, we have investigated the impact of changing the halide ratio on the structure and photostability of $MAPb(I_{1-x}Br_x)_3$ films, exploring an exceptionally fine-grained compositional space. We showed that for near-equal iodide-bromide content, two phases of different macrostrain coexist in the film, which seemingly stabilize the material in the absence of light. Such effects may thus mitigate the possibility of a miscibility gap previously proposed in the literature [47, 48, 53]. Once illuminated, such compositions near $x = 0.5$ also exhibit halide segregation that evolves with two different rate constants, indicating that initial strain engineering via compositional tuning has the potential to modulate photostability. Intriguingly, we observed that the average rate of structural rearrangement caused by halide segregation did not vary across the entire compositional space explored. We postulate that the rate at which segregation can proceed is mostly limited by the mobility of halide ions. We further revealed that the volume fraction of structural rearrangements associated with halide segregation follows a broad Gaussian distribution in compositional space, centered near $x = 0.5$. However, diverging sharply from such underlying trends, the "special" compositions of $MAPbIBr_2$ and $MAPbI_2Br$ present particularly stable and unstable scenarios, respectively. The formation of an ordered phase can thus materially impact the degree of halide segregation. Combining XRD analysis with PL measurements, we were further able to evidence that some amount of halide segregation still occurs below the widely quoted threshold of x equal to 0.2.

Overall, our fine-grained compositional study of a prototypical mixed-halide perovskite, utilizing X-ray structural probes under in situ illumination, provides guidance for proposed models for the mechanism driving halide segregation and identifies possible routes to fabricating segregation-resistant materials. We suggest that further research may target lattice-induced compression via compositional engineering or substrate lattice matching to increase the activation energy for halide migration and thus limit the overall segregation rate [51, 80, 85]. Moreover, we propose that controlling and utilizing strain has clear potential to reduce thermodynamic instabilities driving both initial film (im)miscibility and halide segregation [76]. In addition, our results demonstrate that the extent of halide segregation in mixed-halide films can be modulated by local ordering of the lattice. Therefore, the utilization of special phases that facilitate such ordering, such as for $MAPbIBr_2$ here, may prove highly fruitful to enhance lattice stability. This work will ultimately enable stable bandgap tuning of MHPs, a key requirement for the successful implementation of multijunction perovskite-based solar cell architectures.

5 | Methods

5.1 | Sample Fabrication

$MAPb(I_{1-x}Br_x)_3$ thin films were prepared using the acetonitrile route as reported previously [64, 97]. In brief, MAI (Greatcell), MABr (Greatcell), PbI_2 (TCI Chemicals 99.99%), and $PbBr_2$ (Thermo Scientific 98%) were weighed out and dissolved in a methylamine/acetonitrile (Merck Chemicals) solvent system to give a 0.5 M perovskite solution as described by Noel et al. [97]. The solutions were then statically spin-coated onto z-cut quartz substrates (13 mm diameter) in a nitrogen filled drybox at 2000 rpm for 45 s. The films were then annealed for 90 min at 100°C. For encapsulated thin films, PMMA (poly(methyl methacrylate), Sigma-Aldrich, mean molecular weight $120\,000\ \mathrm{g\,M^{-1}}$) was dissolved in chlorobenzene at $150\ \mathrm{mg\,mL^{-1}}$, and then, 75 µL of solution was statically deposited onto a substrate at a speed of 2000 rpm, $2000\ \mathrm{rpm\,s^{-1}}$ acceleration, for 30 s. After spin coating of PMMA, films were ready to use without further annealing. Unless otherwise specified, all samples were encapsulated with PMMA. All films were stored in a lidded box within a nitrogen-filled glovebox prior to experiment.

5.2 | XRD Measurements Investigating Structural Macrostrain

Unless otherwise specified, XRD patterns assessing structural macrostrain were acquired with a Panalytical X'Pert diffractometer using the Cu-Kα_1 line. A substrate reference peak (z-cut quartz) was utilized to correct for any angular tilt.

5.3 | XRD Measurements Under Illumination

As described in more detail previously [37], a custom-built sample stage was utilized to measure XRD profiles under in situ illumination, mounted inside a Rigaku SmartLab X-ray diffractometer. The incident X-ray radiation used was the Cu-Kα_1 line. A 2D X-ray detector (HyPix-3000) allowed for continual measurement across a fixed 2θ range—the second-order diffraction peak was selected to increase angular resolution, while maintaining sufficient signal intensity. Optical illumination was provided by a fiber-coupled 470 nm diode laser (PicoQuant LDH-D-C-470). After being routed to the sample stage via an optical fiber, laser light was launched into free space toward the thin film (illuminating the thin film side of the sample). Photoluminescence could be collected in parallel by collimation into a second fiber which was connected to an external spectrometer (Ocean Optics USB2000). The illumination spot size was selected such that it was significantly larger than the X-ray probe (Figure S15). The X-ray beam was shaped as a line profile (parallel to the sample surface). At the sample position, the line profile (localized at the center of the illumination spot) followed a Gaussian function with a standard deviation of 0.26 cm. Modeled with a Gaussian function, the optical beam had a standard deviation of 1.2 cm. When projected onto the thin film at 45° to the surface normal, the intensity at the center of the laser excitation (i.e., the locality of the X-ray probe) was calculated to be $0.91\ \mathrm{mW\,cm^{-2}}$ (total laser power of 12 mW). Across the width of the X-ray beam and sample, Gaussian drop-off caused a variation in local laser intensity of less than 15%. Prior to measurement, samples had never been previously exposed to light (except during initial deposition) and were transferred to the diffractometer wrapped in foil, and the diffractometer was shielded from all other external light during the measurement.

Author Contributions

Joshua R. S. Lilly: conceptualization (supporting), data curation (lead), formal analysis (lead), investigation (lead), writing – original draft (lead), writing – review and editing (equal). **Vincent J.-Y. Lim:** data curation (supporting), formal analysis (supporting), investigation (supporting), supervision (supporting), writing – original draft (supporting), writing review and editing (supporting). **Jay B. Patel:** data curation (supporting), formal analysis (supporting), methodology (supporting), resources (supporting). **Siyu Yan:** data curation (supporting), formal analysis (supporting), methodology (supporting). **Jae Eun Lee:** data curation (supporting), formal analysis (supporting), methodology (supporting). **Michael B. Johnston:** conceptualization (supporting), data curation (supporting), funding acquisition (equal), supervision (equal), writing – review and editing (supporting). **Laura M. Herz:** conceptualization (lead), data curation (supporting), formal analysis (supporting), funding acquisition (lead), investigation (supporting), methodology (lead), project administration (lead), resources (lead), supervision (lead), validation (lead), writing – original draft (equal), writing – review and editing (lead).

Acknowledgments

The authors thank the Engineering and Physical Sciences Research Council (EPSRC) for financial support, including through EPSRC grants EP/Y014952/1 and EP/X038777/1. J.B.P. acknowledges support through EPSRC grant EP/W007975/2. J.R.S.L. thanks Oxford Photovoltaics for additional support as part of an EPSRC Industrial CASE studentship. V.J.Y.L. acknowledges funding through an EPSRC Doctoral Prize.

Conflicts of Interest

The authors declare no conflicts of interest.

Data Availability Statement

The data that support the findings of this study are available from the corresponding author upon reasonable request.

References

1. A. Kojima, K. Teshima, Y. Shirai, and T. Miyasaka, “Organometal Halide Perovskites as Visible-Light Sensitizers for Photovoltaic Cells,” *Journal of the American Chemical Society* 131 (2009): 6050.

2. M. Liu, M. B. Johnston, and H. J. Snaith, “Efficient Planar Heterojunction Perovskite Solar Cells by Vapour Deposition,” *Nature* 501 (2013): 395.

3. J. P. Mailoa, C. D. Bailie, E. C. Johlin, et al., “A 2-Terminal Perovskite/Silicon Multijunction Solar Cell Enabled by a Silicon Tunnel Junction,” *Applied Physics Letters* 106 (2015): 121105.

4. Z.-K. Tan, R. S. Moghaddam, M. L. Lai, et al., “Bright Light-Emitting Diodes Based on Organometal Halide Perovskite,” *Nature Nanotechnology* 9 (2014): 687.

5. S. Yakunin, M. Sytnyk, D. Kriegner, et al., “Detection of X-Ray Photons by Solution-Processed Lead Halide Perovskites,” *Nature Photonics* 9 (2015): 444.

6. G. Xing, N. Mathews, S. S. Lim, et al., “Low-Temperature Solution-Processed Wavelength-Tunable Perovskites for Lasing,” *Nature Materials* 13 (2014): 476.

7. F. Deschler, M. Price, S. Pathak, et al., “High Photoluminescence Efficiency and Optically Pumped Lasing in Solution-Processed Mixed Halide Perovskite Semiconductors,” *The Journal of Physical Chemistry Letters* 5 (2014): 1421.

8. L. Dou, Y. Yang, J. You, et al., “Solution-Processed Hybrid Perovskite Photodetectors with High Detectivity,” *Nature Communications* 5 (2014): 5404.

9. NREL, “*Best Research-Cell Efficiency Chart*,” Accessed March 5th, 2025, https://www.nrel.gov/pv/cell-efficiency.html.

10. S. D. Stranks, G. E. Eperon, G. Grancini, et al., “Electron-Hole Diffusion Lengths Exceeding 1 Micrometer in an Organometal Trihalide Perovskite Absorber,” *Science* 342 (2013): 341.

11. C. Wehrenfennig, G. E. Eperon, M. B. Johnston, H. J. Snaith, and L. M. Herz, “High Charge Carrier Mobilities and Lifetimes in Organolead Trihalide Perovskites,” *Advanced Materials* 26 (2014): 1584.

12. L. M. Herz, “Charge-Carrier Mobilities in Metal Halide Perovskites: Fundamental Mechanisms and Limits,” *ACS Energy Letters* 2 (2017): 1539.

13. M. B. Johnston and L. M. Herz, “Hybrid Perovskites for Photovoltaics: Charge-Carrier Recombination, Diffusion, and Radiative Efficiencies,” *Accounts of Chemical Research* 49 (2016): 146.

14. C. L. Davies, M. R. Filip, J. B. Patel, et al., “Bimolecular Recombination in Methylammonium Lead Triiodide Perovskite Is an Inverse Absorption Process,” *Nature Communications* 9 (2018): 293.

15. D. W. deQuilettes, J. J. Yoo, R. Brenes, et al., “Reduced Recombination via Tunable Surface Fields in Perovskite Thin Films,” *Nature Energy* 9 (2024): 457.

16. L. M. Herz, “Charge-Carrier Dynamics in Organic-Inorganic Metal Halide Perovskites,” *Annual Review of Physical Chemistry* 67 (2016): 65.

17. T. Leijtens, K. A. Bush, R. Prasanna, and M. D. McGehee, “Opportunities and Challenges for Tandem Solar Cells Using Metal Halide Perovskite Semiconductors,” *Nature Energy* 3 (2018): 828.

18. E. L. Unger, L. Kegelmann, K. Suchan, D. Sörell, L. Korte, and S. Albrecht, “Roadmap and Roadblocks for the Band Gap Tunability of Metal Halide Perovskites,” *Journal of Materials Chemistry A* 5 (2017): 11401.

19. F. Hao, C. C. Stoumpos, R. P. H. Chang, and M. G. Kanatzidis, “Anomalous Band Gap Behavior in Mixed Sn and Pb Perovskites Enables Broadening of Absorption Spectrum in Solar Cells,” *Journal of the American Chemical Society* 136 (2014): 8094.

20. K. J. Savill, A. M. Ulatowski, and L. M. Herz, “Optoelectronic Properties of Tin–Lead Halide Perovskites,” *ACS Energy Letters* 6 (2021): 2413.

21. J. H. Noh, S. H. Im, J. H. Heo, T. N. Mandal, and S. I. Seok, “Chemical Management for Colorful, Efficient, and Stable Inorganic–Organic Hybrid Nanostructured Solar Cells,” *Nano Letters* 13 (2013): 1764.

22. D. P. McMeekin, G. Sadoughi, W. Rehman, et al., “A Mixed-Cation Lead Mixed-Halide Perovskite Absorber for Tandem Solar Cells,” *Science* 351 (2016): 151.

23. M. C. Brennan, A. Ruth, P. V. Kamat, and M. Kuno, “Photoinduced Anion Segregation in Mixed Halide Perovskites,” *Trends in Chemistry* 2 (2020): 282.

24. L. Protesescu, S. Yakunin, M. I. Bodnarchuk, et al., “Nanocrystals of Cesium Lead Halide Perovskites (CsPbX3, X = Cl, Br, and I): Novel Optoelectronic Materials Showing Bright Emission with Wide Color Gamut,” *Nano Letters* 15 (2015): 3692.

25. L. Yang, W.-L. Tsai, C.-S. Li, et al., “High-Quality Conformal Homogeneous All-Vacuum Deposited CsPbCl3 Thin Films and Their UV Photodiode Applications,” *ACS Applied Materials & Interfaces* 11 (2019): 47054.

26. Y. J. Ahn, H. J. Kim, I. J. Park, and J. Y. Kim, “Recent Advances and Opportunities in Perovskite-Based Triple-Junction Tandem Solar Cells,” *Sustainable Energy Fuels* 8 (2024): 5352.

27. S. Hu, J. Wang, P. Zhao, et al., “Steering Perovskite Precursor Solutions for Multijunction Photovoltaics,” *Nature* 639 (2025): 93.

28. H. Li and W. Zhang, “Perovskite Tandem Solar Cells: From Fundamentals to Commercial Deployment,” *Chemical Reviews* 120 (2020): 9835.

29. Z. Wang, L. Zeng, T. Zhu, et al., “Suppressed Phase Segregation for Triple-Junction Perovskite Solar Cells,” *Nature* 618 (2023): 74.

30. J. Liu, Y. He, L. Ding, et al., “Perovskite/Silicon Tandem Solar Cells with Bilayer Interface Passivation,” *Nature* 635 (2024): 596.

31. M. Heydarian, M. Heydarian, A. J. Bett, et al., “Monolithic Two-Terminal Perovskite/Perovskite/Silicon Triple-Junction Solar Cells with Open Circuit Voltage > 2.8 V,” *ACS Energy Letters* 8 (2023): 4186.

32. X. Luo and E. L. Lim, “A Mini-Review: The Rise of Triple-Junction Silicon-Perovskite-Perovskite Solar Cells,” *Solar RRL* 9 (2025): 2400730.

33. S. P. Philipps and A. W. Bett, “III-V Multi-Junction Solar Cells and Concentrating Photovoltaic (CPV) Systems,” *Advanced Optical Technologies* 3 (2014): 469.

34. E. T. Hoke, D. J. Slotcavage, E. R. Dohner, A. R. Bowring, H. I. Karunadasa, and M. D. McGehee, “Reversible Photo-Induced Trap Formation in Mixed-Halide Hybrid Perovskites for Photovoltaics,” *Chemical Science* 6 (2015): 613.

35. I. L. Braly, R. J. Stoddard, A. Rajagopal, et al., "Current-Induced Phase Segregation in Mixed Halide Hybrid Perovskites and Its Impact on Two-Terminal Tandem Solar Cell Design," *ACS Energy Letters* 2 (2017): 1841.

36. C. G. Bischak, C. L. Hetherington, H. Wu, et al., "Origin of Reversible Photoinduced Phase Separation in Hybrid Perovskites," *Nano Letters* 17 (2017): 1028.

37. A. J. Knight, J. Borchert, R. D. J. Oliver, et al., "Halide Segregation in Mixed-Halide Perovskites: Influence of A-Site Cations," *ACS Energy Letters* 6 (2021): 799.

38. W. Rehman, D. P. McMeekin, J. B. Patel, et al., "Photovoltaic Mixed-Cation Lead Mixed-Halide Perovskites: Links Between Crystallinity, Photo-Stability and Electronic Properties," *Energy & Environmental Science* 10 (2017): 361.

39. A. D. Wright, Jay B. Patel, M. B. Johnston, and L. M. Herz, "Temperature-Dependent Reversal of Phase Segregation in Mixed-Halide Perovskites," *Advanced Materials* 35 (2023): 2210834.

40. S. G. Motti, J. B. Patel, R. D. J. Oliver, H. J. Snaith, M. B. Johnston, and L. M. Herz, "Phase Segregation in Mixed-Halide Perovskites Affects Charge-Carrier Dynamics While Preserving Mobility," *Nature Communications* 12 (2021): 6955.

41. Y. Zhou, E. L. Wong, W. Mróz, et al., "Role of Trapped Carriers Dynamics in Operating Lead Halide Wide-Bandgap Perovskite Solar Cells," *ACS Energy Letters* 9 (2024): 1666.

42. G. C. Halford, Q. Deng, A. Gomez, T. Green, J. M. Mankoff, and R. A. Belisle, "Structural Dynamics of Metal Halide Perovskites during Photoinduced Halide Segregation," *ACS Applied Materials & Interfaces* 14 (2022): 4335.

43. S. Draguta, O. Sharia, S. J. Yoon, et al., "Rationalizing the Light-Induced Phase Separation of Mixed Halide Organic–Inorganic Perovskites," *Nature Communications* 8 (2017): 200.

44. C. G. Bischak, A. B. Wong, E. Lin, D. T. Limmer, P. Yang, and N. S. Ginsberg, "Tunable Polaron Distortions Control the Extent of Halide Demixing in Lead Halide Perovskites," *The Journal of Physical Chemistry Letters* 9 (2018): 3998.

45. T. Zhu, L. Grater, S. Teale, et al., "Coupling Photogeneration with Thermodynamic Modeling of Light-Induced Alloy Segregation Enables the Identification of Stabilizing Dopants," *Chemistry of Materials : A Publication of the American Chemical Society* 36 (2024): 7438.

46. A. J. Knight and L. M. Herz, "Preventing Phase Segregation in Mixed-Halide Perovskites: A Perspective," *Energy & Environmental Science* 13 (2020): 2024.

47. F. Brivio, C. Caetano, and A. Walsh, "Thermodynamic Origin of Photoinstability in the CH3NH3Pb(I1–xBrx)3 Hybrid Halide Perovskite Alloy," *The Journal of Physical Chemistry Letters* 7 (2016): 1083.

48. F. Lehmann, A. Franz, D. M. Többens, et al., "The Phase Diagram of a Mixed Halide (Br, I) Hybrid Perovskite Obtained by Synchrotron X-Ray Diffraction," *RSC Advances* 9 (2019): 11151.

49. K. Suchan, J. Just, P. Beblo, et al., "Multi-Stage Phase-Segregation of Mixed Halide Perovskites under Illumination: A Quantitative Comparison of Experimental Observations and Thermodynamic Models," *Advanced Functional Materials* 33 (2023): 2206047.

50. Y. Zhao, P. Miao, J. Elia, et al., "Strain-Activated Light-Induced Halide Segregation in Mixed-Halide Perovskite Solids," *Nature Communications* 11 (2020): 6328.

51. L. A. Muscarella, E. M. Hutter, F. Wittmann, et al., "Lattice Compression Increases the Activation Barrier for Phase Segregation in Mixed-Halide Perovskites," *ACS Energy Letters* 5 (2020): 3152.

52. P. Fedeli, F. Gazza, D. Calestani, et al., "Influence of the Synthetic Procedures on the Structural and Optical Properties of Mixed-Halide (Br, I) Perovskite Films," *Journal of Physical Chemistry C* 119 (2015): 21304.

53. D. Liu, D. Luo, A. N. Iqbal, et al., "Strain Analysis and Engineering in Halide Perovskite Photovoltaics," *Nature Materials* 20 (2021): 1337.

54. M. Wang, Y. Lu, X. Huo, et al., "Mitigating Lattice Strain and Phase Segregation of Mixed-Halide Perovskite Films via Dual Chloride Additive Strategy toward Highly Efficient and Stable Perovskite Solar Cells," *Journal of Power Sources* 561 (2023): 232753.

55. W.-J. Yin, Y. Yan, and S.-H. Wei, "Anomalous Alloy Properties in Mixed Halide Perovskites," *The Journal of Physical Chemistry Letters* 5 (2014): 3625.

56. E. M. Hutter, L. A. Muscarella, F. Wittmann, et al., "Thermodynamic Stabilization of Mixed-Halide Perovskites against Phase Segregation," *Cell Reports Physical Science* 1 (2020): 100120.

57. L. A. Muscarella and B. Ehrler, "The Influence of Strain on Phase Stability in Mixed-Halide Perovskites," *Joule* 6 (2022): 2016.

58. R. A. Kerner, Z. Xu, B. W. Larson, and B. P. Rand, "The Role of Halide Oxidation in Perovskite Halide Phase Separation," *Joule* 5 (2021): 2273.

59. Z. Xu, R. A. Kerner, J. J. Berry, and B. P. Rand, "Iodine Electrochemistry Dictates Voltage-Induced Halide Segregation Thresholds in Mixed-Halide Perovskite Devices," *Advanced Functional Materials* 32 (2022): 2203432.

60. Z. Xu, X. Zhong, T. Hu, J. Hu, A. Kahn, and B. P. Rand, "Correlating Halide Segregation with Photolysis in Mixed-Halide Perovskites via In Situ Opto-Gravimetric Analysis," *Journal of the American Chemical Society* 146 (2024): 33368.

61. S. Martani, Y. Zhou, I. Poli, et al., "Defect Engineering to Achieve Photostable Wide Bandgap Metal Halide Perovskites," *ACS Energy Letters* 8 (2023): 2801.

62. Y. Zhou, S. C. W. van Laar, D. Meggiolaro, et al., "How Photogenerated I2 Induces I-Rich Phase Formation in Lead Mixed Halide Perovskites," *Advanced Materials* 36 (2024): 2305567.

63. A. J. Knight, A. D. Wright, J. B. Patel, et al., "Electronic Traps and Phase Segregation in Lead Mixed-Halide Perovskite," *ACS Energy Letters* 4 (2019): 75.

64. A. J. Knight, J. B. Patel, H. J. Snaith, M. B. Johnston, and L. M. Herz, "Trap States, Electric Fields, and Phase Segregation in Mixed-Halide Perovskite Photovoltaic Devices," *Advanced Energy Materials* 10 (2020): 1903488.

65. W. Mao, C. R. Hall, S. Bernardi, et al., "Light-Induced Reversal of Ion Segregation in Mixed-Halide Perovskites," *Nature Materials* 20 (2021): 55.

66. D. T. Limmer and N. S. Ginsberg, "Photoinduced Phase Separation in the Lead Halides Is a Polaronic Effect," *The Journal of Chemical Physics* 152 (2020): 230901.

67. A. Ruth, H. Okrepka, P. Kamat, and M. Kuno, "Thermodynamic Band Gap Model for Photoinduced Phase Segregation in Mixed-Halide Perovskites," *Journal of Physical Chemistry C* 127 (2023): 18547.

68. Z. Chen, G. Brocks, S. Tao, and P. A. Bobbert, "Unified Theory for Light-Induced Halide Segregation in Mixed Halide Perovskites," *Nature Communications* 12 (2021): 2687.

69. L. McGovern, G. Grimaldi, M. H. Futscher, et al., "Reduced Barrier for Ion Migration in Mixed-Halide Perovskites," *ACS Applied Energy Materials* 4 (2021): 13431.

70. J. E. Lee, M. Righetto, B. W. J. Putland, et al., "Impact of Charge Transport Layers on the Structural and Optoelectronic Properties of Coevaporated Cu2AgBiI6," *ACS Applied Materials & Interfaces* 17 (2025): 40363.

71. N. K. Noel, B. Wenger, S. N. Habisreutinger, et al., "Highly Crystalline Methylammonium Lead Tribromide Perovskite Films for Efficient Photovoltaic Devices," *ACS Energy Letters* 3 (2018): 1233.

72. G. F. Harrington and J. Santiso, "Back-to-Basics Tutorial: X-Ray Diffraction of Thin Films," *Journal of Electroceramics* 47 (2021): 141.

73. W. L. Tan and C. R. McNeill, “X-Ray Diffraction of Photovoltaic Perovskites: Principles and Applications,” *Applied Physics Reviews* 9 (2022): 021310.

74. I. G. Hughes and T. P. A. Hase, *Measurements and Their Uncertainties: A Practical Guide to Modern Error Analysis* (Oxford University Press, 2010).

75. P. Shi, J. Xu, I. Yavuz, et al., “Strain Regulates the Photovoltaic Performance of Thick-Film Perovskites,” *Nature Communications* 15 (2024): 2579.

76. G. B. Stringfellow, “Spinodal Decomposition and Clustering in III/V Alloys,” *Journal of Electronic Materials* 11 (1982): 903.

77. D. Chu, B. Jia, N. Liu, et al., “Lattice Engineering for Stabilized Black FAPbI3 Perovskite Single Crystals for High-Resolution X-Ray Imaging at the Lowest Dose,” *Science Advances* 9 (2023): eadh2255.

78. S. Porwal, N. K. Bansal, S. Ghosh, and T. Singh, “Stress-Induced Stabilization of the Photoactive FAPbI3 Phase under Ambient Conditions without Using an Additive Approach,” *Energy Advances* 3 (2024): 894.

79. M. Lv, N. Li, G. Jin, X. Du, X. Tao, and Z. Chen, “Phase-Stable FAPbI3-Based Single Crystals with 600-μm Electron Diffusion Length,” *Matter* 6 (2023): 4388.

80. J. S. Solomon, T. Soto-Montero, Y. A. Birkhölzer, et al., “Room-Temperature Epitaxy of α-CH3NH3PbI3 Halide Perovskite by Pulsed Laser Deposition,” *Nature Synthesis* 4 (2025): 432.

81. W. Li, Q. Yuan, Y. Chen, et al., “Ruddlesden–Popper Defects Act as a Free Surface: Role in Formation and Photophysical Properties of CsPbI3,” *Advanced Materials* 37, no. 34 (2025): 2501788.

82. V. J.-Y. Lim, A. J. Knight, R. D. J. Oliver, H. J. Snaith, M. B. Johnston, and L. M. Herz, “Impact of Hole-Transport Layer and Interface Passivation on Halide Segregation in Mixed-Halide Perovskites,” *Advanced Functional Materials* 32 (2022): 2204825.

83. M. E. Stuckelberger, T. Nietzold, B. M. West, et al., “Effects of X-Rays on Perovskite Solar Cells,” *Journal of Physical Chemistry C* 124 (2020): 17949.

84. J. E. Lee, S. G. Motti, R. D. J. Oliver, et al., “Unraveling Loss Mechanisms Arising from Energy-Level Misalignment Between Metal Halide Perovskites and Hole Transport Layers,” *Advanced Functional Materials* 34 (2024): 2401052.

85. G. Sarkar and D. Ghosh, “Effects of Lattice Compression on Halogen Ion Diffusion Dynamics in Mixed Halide Perovskites,” *ACS Applied Energy Materials* 7 (2024): 6376.

86. F. P. Sabino, G. M. Dalpian, and A. Zunger, “Light-Induced Frenkel Defect Pair Formation Can Lead to Phase-Segregation of Otherwise Miscible Halide Perovskite Alloys,” *Advanced Energy Materials* 13 (2023): 2301539.

87. Q. Fan, Y. Cui, Y. Li, et al., “Phase Segregation Dynamics in Mixed-Halide Perovskites Revealed by Plunge-Freeze Cryo-Electron Microscopy,” *Cell Reports Physical Science* 6 (2025): 102653.

88. Y. Hong, C. Yu, H. Je, et al., “Perovskite Nanocrystals Protected by Hermetically Sealing for Highly Bright and Stable Deep-Blue Light-Emitting Diodes,” *Advancement of Science* 10 (2023): 2302906.

89. K. A. Bush, K. Frohna, R. Prasanna, et al., “Compositional Engineering for Efficient Wide Band Gap Perovskites with Improved Stability to Photoinduced Phase Segregation,” *ACS Energy Letters* 3 (2018): 428.

90. M. Safdari, D. Kim, A. Balvanz, and M. G. Kanatzidis, “Mitigation of Halide Segregation by Cation Composition Management in Wide Bandgap Perovskites,” *ACS Energy Letters* 9 (2024): 3400.

91. A. Ruth and M. Kuno, “Modeling the Photoelectrochemical Evolution of Lead-Based, Mixed-Halide Perovskites Due to Photosegregation,” *ACS Nano* 17 (2023): 20502.

92. Y. Guo, C. Zhang, L. Wang, et al., “Unveiling the Impact of Photoinduced Halide Segregation on Performance Degradation in Wide-Bandgap Perovskite Solar Cells,” *Energy & Environmental Science* 18 (2025): 2308.

93. R. J. Stoddard, A. Rajagopal, R. L. Palmer, I. L. Braly, A. K.-Y. Jen, and H. W. Hillhouse, “Enhancing Defect Tolerance and Phase Stability of High-Bandgap Perovskites via Guanidinium Alloying,” *ACS Energy Letters* 3 (2018): 1261.

94. A. F. Palmstrom, G. E. Eperon, T. Leijtens, et al., “Enabling Flexible All-Perovskite Tandem Solar Cells,” *Joule* 3 (2019): 2193.

95. S. Liu, Y. Lu, C. Yu, et al., “Triple-Junction Solar Cells with Cyanate in Ultrawide-Bandgap Perovskites,” *Nature* 628 (2024): 306.

96. S. Yan, J. B. Patel, J. E. Lee, et al., “A Templating Approach to Controlling the Growth of Coevaporated Halide Perovskites,” *ACS Energy Letters* 8 (2023): 4008.

97. N. K. Noel, S. N. Habisreutinger, B. Wenger, et al., “A Low Viscosity, Low Boiling Point, Clean Solvent System for the Rapid Crystallisation of Highly Specular Perovskite Films,” *Energy & Environmental Science* 10 (2017): 145.

Supporting Information

Additional supporting information can be found online in the Supporting Information section. **Supporting Fig. S1:** Image of $\mathrm{MAPb(I_{1-x}Br_x)_3}$ thin films on z-cut quartz substrates. **Supporting Fig. S2:** X-ray diffraction patterns for $\mathrm{MAPb(I_{1-x}Br_x)_3}$ thin films on z-cut quartz substrates. **Supporting Fig. S3:** Absorbance spectra of the $\mathrm{MAPb(I_{1-x}Br_x)_3}$ thin film with a nominal bromide fraction of $x = 0.55$. **Supporting Fig. S4:** Second-order diffraction peak for $\mathrm{MAPb(I_{1-x}Br_x)_3}$ thin films on z-cut quartz substrates. Data is modelled with a single Voigt profile. **Supporting Fig. S5:** Minimised reduced χ^2 ($\chi_\nu{}^2$) when either a single Voigt profile or the sum of two Voigt profiles are used to model the (200) diffraction peak. **Supporting Fig. S6:** Second-order diffraction peak for a $\mathrm{MAPbBr_3}$ thin film. **Supporting Fig. S7:** Durbin-Watson statistic for the two cases of using a single Voigt profile and the sum of two Voigt profiles to model the (200) diffraction peak. **Supporting Fig. S8:** Improvement in the Durbin-Watson statistic when moving from fits based on a single Voigt profile to those based on the sum of two Voigt profiles to model the (200) diffraction peak. **Supporting Fig. S9:** Second-order diffraction peak for $\mathrm{MAPb(I_{1-x}Br_x)_3}$ thin films. Data is modelled with the sum of two Voigt profiles. **Supporting Fig. S10:** Second-order diffraction peak for $\mathrm{MAPb(I_{1-x}Br_x)_3}$ thin films before and after 16 h of illumination with a constant intensity of 0.91 mW cm^{-2} via a 470 nm continuous wave laser excitation. **Supporting Fig. S11:** Area underneath the second-order diffraction peak for $\mathrm{MAPb(I_{1-x}Br_x)_3}$ thin films normalised to the initial peak area. **Supporting Fig. S12:** Relative structural change in thin films of $\mathrm{MAPb(I_{1-x}Br_x)_3}$ arising from halide segregation. **Supporting Fig. S13:** Reduced minimised χ^2 ($\chi_\nu{}^2$) for the three cases of using a monoexponential function, a biexponential function, and the sum of a monoexponential function and a linear function (constrained to go through the origin) to model the relative structural change. **Supporting Fig. S14:** Relative structural change as a function of illumination time, extracted for two different $\mathrm{MAPb(I_{1-x}Br_x)_3}$ thin-film samples of the same nominal bromide content x, evidencing minimal sample-to-sample variation for identical composition. **Supporting Fig. S15:** Profile of the X-ray beam and laser excitation. **Supporting Fig. S16:** Second-order diffraction peak for three $\mathrm{MAPb(I_{1-x}Br_x)_3}$ thin films of different nominal bromide fraction x, prepared as part of a separate batch. **Supporting Fig. S17:** Second-order diffraction peak for $\mathrm{MAPb(I_{1-x}Br_x)_3}$ thin films recorded on a different diffractometer. **Supporting Fig. S18:** Ratio of the minimised reduced χ^2 ($\chi_\nu{}^2$) when moving from the use of a single Voigt profile to the use of the sum of two Voigt profiles to model the (200) diffraction peak for $\mathrm{MAPb(I_{1-x}Br_x)_3}$ thin-film samples on z-cut quartz presented in Figure S17. **Supporting Fig. S19:** Second-order diffraction peak for $\mathrm{MAPb(I_{1-x}Br_x)_3}$ thin films with PMMA encapsulant . **Supporting Fig. S20:** Ratio of the minimised reduced χ^2 ($\chi_\nu{}^2$) when moving from the use of a single Voigt profile to the use of the sum of two Voigt profiles to model the (200) diffraction peak for $MAPb(I_{1-x}Br_x)_3$ thin-film samples on z-cut quartz presented in Figure S19. **Supporting Fig. S21:** Centres of second-order X-ray diffraction peaks for $MAPb(I_{1-x}Br_x)_3$ thin films, extracted from modelling with a single Voigt profile and the sum of two Voigt profiles. **Supporting Fig. S22:** Second-order diffraction peak for $MAPb(I_{1-x}Br_x)_3$ thin films prepared as part of a separate batch. This batch used a shorter annealing time. **Supporting Fig. S23:** Second-order diffraction peak for $MAPb(I_{1-x}Br_x)_3$ thin films that had previously been exposed to continuous light-soaking and then had been allowed to remix in the dark. **Supporting Fig. S24:** Ratio of the minimised reduced χ^2 ($\chi_v{}^2$) when moving from the use of a single Voigt profile to the use of the sum of two Voigt profiles to model the (200) diffraction peak for $MAPb(I_{1-x}Br_x)_3$ thin-film samples on z-cut quartz presented in Figure S23. **Supporting Fig. S25:** Intensity difference for the (200) diffraction peak after 16 h of continuous illumination (with respect to the peak obtained before illumination) for a composition with a nominal bromide fraction of 0.25. **Supporting Fig. S26:** Example correction procedure for the relative structural change as a function of illumination time for a composition with a nominal bromide fraction of 0. **Supporting Fig. S27:** Example correction procedure for the relative structural change as a function of illumination time for a $MAPb(I_{1-x}Br_x)_3$ composition with a nominal bromide fraction of 0.3. **Supporting Fig. S28:** Example extraction of the average rate of structural change. **Supporting Table S1:** Table summarising the results of the study and proposed design strategies to enhance the stability of different multi-junction perovskite-based solar cell architectures. **Supporting Note S1:** Further discussion of diffraction peak asymmetry. **Supporting Note S2:** Experimental design. **Supporting Note S3:** Calculating the relative structural change. **Supporting Note S4:** Extracting average rate of structural change.